

# An Artificial Potential Field based Sampling Strategy for a Gas-Sensitive Micro-Drone

Patrick Neumann, Sahar Asadi, Jochen H. Schiller, Achim Lilienthal and Matthias Bartholmai

**Abstract**— This paper presents a sampling strategy for mobile gas sensors. Sampling points are selected using a modified artificial potential field (APF) approach, which balances multiple criteria to direct sensor measurements towards locations of high mean concentration, high concentration variance and areas for which the uncertainty about the gas distribution model is still large. By selecting in each step the *most often suggested close-by* measurement location, the proposed approach introduces a locality constraint that allows planning suitable paths for mobile gas sensors. Initial results in simulation and in real-world experiments with a gas-sensitive micro-drone demonstrate the suitability of the proposed sampling strategy for gas distribution mapping and its use for gas source localization.

**Index Terms**—autonomous UAV, chemical sensing, gas distribution modelling, gas source localization, gas sensors, mobile sensing system, quadcopter, sensor planning, artificial potential field.

## I. INTRODUCTION

Gas distribution modelling and gas source localization play an important role in environmental management applications such as leak detection and landfill monitoring [1], for example. The response of many gas sensors, however, is caused by direct interaction with the chemical compounds and thus represents only a small area around the sensor surface. For practical applications either a large number of stationary sensors or mobile sensors are required. In this paper we consider the case of gas sensors carried by a mobile robot, which offers a number of advantages including rapid deployment, adaptation to changing environmental conditions, and the possibility to move to areas of high concentration, to name but a few. A crucial element for gas-sensitive mobile robots is a sensor planning strategy that selects preferable sampling locations based on the current knowledge about the environment and more specifically the current knowledge about the gas distribution. The purpose of

the sensor planning component is to reduce the time that is necessary to converge to the final gas distribution model or to reliably identify important parameters of the distribution such as areas of high concentration, for example. Sensor planning is especially important in the case of a flying gas-sensitive robot such as the one considered in this paper due to its limited battery life time.

In this paper, we adapt a newly developed sensor planning approach by introducing locality constraints to plan the path for a micro-drone. The sensor planning algorithm uses information about the target area and previous sampling locations. In addition, it considers the current statistical gas distribution model to direct sensor measurements towards locations of high mean concentration, high concentration variance and areas for which the uncertainty about the gas distribution model is still large. The different objectives are combined in an Artificial Potential Field (APF) in a way that allows to include additional objectives, e.g. from human operators, in an intuitive and straightforward way. In addition to the introduction of the modified APF-based sensor planning algorithm and the demonstration on a gas-sensitive micro-drone, we also demonstrate that the peak in the predictive variance model can provide an accurate estimation of the location of a stationary gas source.

In the remainder of this paper, we first describe the APF-based approach for sensor planning and its modification to provide meaningful search paths for a mobile gas sensor (Sec. II). Next, we describe the robotic platform used (Sec. III) and the experimental set-up (Sec. IV). Finally we present the results (Sec. V), draw conclusions and identify directions of future work (Sec. VI).

## II. SENSOR AND PATH PLANNING

### A. Statistical Gas Distribution Modelling

The first step in the proposed algorithm is to create a statistical gas distribution model using the Kernel DM+V/W algorithm introduced by Reggente and Lilienthal [6]. The input to this algorithm is a set of measurements  $D = \{(x_1, r_1, v_1), \dots, (x_n, r_n, v_n)\}$  with gas sensor measurements  $r_i$  and airflow measurements  $v_i$  collected at locations  $x_i$ . The output is a grid model that computes an estimate of distribution mean and variance for each cell. We use the 2D version of the Kernel DM+V/W algorithm as basis for the APF sensor planning algorithm to avoid the higher computational complexity of the 3D Kernel DM+V/W algorithm [7] and because of the limited battery capacity of

Manuscript received June 03, 2011. This work was supported by BMWi within the MNPQ programme (file number 28/07) and the EC (contract number FP7-224318-DIADEM).

Patrick Neumann and Matthias Bartholmai work for the BAM Federal Institute for Materials Research and Testing, D – 12205 Berlin, Germany (corresponding author to provide phone: +493081043629; fax: +493081041917; e-mail: Patrick.Neumann@bam.de).

Jochen H. Schiller works for the Institute of Computer Science, FU University, D – 14195 Berlin, Germany.

Achim Lilienthal and Sahar Asadi are members of the AASS Research Centre, School of Science and Technology, Örebro University, SE – 70182 Örebro, Sweden.

the micro-drone, which does not permit a full 3D search. In the experiments, the drone was kept in a single 2D plane.

The Kernel DM+V/W algorithm works as follows. In the first step, it computes weights  $\omega_i^{(k)}$  that model the information content of measurement  $i$  at grid cell  $k$ . This is done by evaluating a two-dimensional, multivariate Gaussian kernel  $N$  at the distance between the location of the measurement  $i$  and the center  $x^{(k)}$  of cell  $k$ :

$$\omega_i^{(k)} = N(|x^{(k)} - x_i|, v; \sigma, \gamma). \quad (1)$$

The shape and orientation of the kernel depends on the local airflow vector  $v$  and on two meta-parameters that determine a spatial scale ( $\sigma$ ) and a wind scale ( $\gamma$ ). If no wind is measured (or if no wind information is available), the Gaussian kernel has a circular shape. In case of a non-zero wind measurement the kernel takes the shape of an elongated ellipse with the semi-major axis rotated in wind direction and stretched according to the strength of the wind.

Second, weights  $\omega_i^{(k)}$ , weighted sensor readings  $\omega_i^{(k)} \cdot r_i$ , and weighted variance contributions  $\omega_i^{(k)} (r_i - r^{(k(i))})^2$  are integrated and stored in temporary grid maps.

$$\Omega^{(k)} = \sum_{i=1}^n \omega_i^{(k)}, \quad (2)$$

$$R^{(k)} = \sum_{i=1}^n \omega_i^{(k)} \cdot r_i, \quad (3)$$

$$V^{(k)} = \sum_{i=1}^n \omega_i^{(k)} \cdot (r_i - r^{(k(i))})^2 \quad (4)$$

The variance contributions are computed using the difference between the actual measurements  $r_i$  and the corresponding prediction of the model  $r^{(k(i))}$ , i.e. the predictive mean for the grid cell  $k(i)$  closest to the point at which  $r_i$  was measured.

Third, a confidence map  $\alpha^{(k)}$  is computed from the integrated weights  $\Omega^{(k)}$  using another scaling parameter  $\sigma_\Omega$  as a soft threshold:

$$\alpha^{(k)} = 1 - e^{-\frac{\Omega^{(k)}}{\sigma_\Omega^2}}. \quad (5)$$

The confidence map expresses an increased confidence at locations for which we have a large number of sensor readings in the close vicinity (“close” is to be understood relative to the kernel width  $\sigma$ ).

Finally, the map estimate of the mean  $r^{(k)}$  and the corresponding variance estimate  $v^{(k)}$  is calculated using (6) and (7) as

$$r^{(k)}(\sigma, \gamma, \sigma_\omega) = \alpha^{(k)} \frac{R^{(k)}}{\Omega^{(k)}} + (1 - \alpha^{(k)}) r_0, \quad (6)$$

$$v^{(k)}(\sigma, \gamma, \sigma_\omega) = \alpha^{(k)} \frac{V^{(k)}}{\Omega^{(k)}} + (1 - \alpha^{(k)}) v_0. \quad (7)$$

The final estimate is obtained by linear interpolation between the map prediction and an *a priori* estimate for cells with low confidence. For the mean, the *a priori* estimate  $r_0$  is computed as the average concentration over all sensor readings. Similarly, the average over all variance contributions  $v_0$  is used to estimate the distribution variance in regions far away from measurement points.

### B. Artificial Potential Field (APF) based Sensor Planning

In each step, the sensor planning component suggests a selectable number  $n_{sp}$  of locations to place sensors in the area of interest in the next iteration. The algorithm uses information about the target area, previous sampling locations, and the current statistical gas distribution model (described in the previous section). The selection process considers three objectives to direct the sensor towards areas of (1) high predictive mean, (2) high predictive variance and (3) areas in which the model uncertainty is high.

The first two objectives implement exploitation of the information in the gas distribution model. They are realized with an attractive potential generated by charges placed in each grid cell center. The strength of these charges is given by the corresponding predictive mean and variance. Accordingly, two APF contributions are computed for each cell  $k$  as

$$APF_M^{(k)} = \sum_{j \neq k} r^{(k)} \cdot e^{-\frac{|x^{(j)} - x^{(k)}|}{\sigma_d}}, \quad (8)$$

$$APF_V^{(k)} = \sum_{j \neq k} v^{(k)} \cdot e^{-\frac{|x^{(j)} - x^{(k)}|}{\sigma_d}}. \quad (9)$$

The third objective that corresponds to exploration is implemented by a repulsive potential generated by placing charges at all  $|D| = n$  previous measurement locations:

$$APF_R^{(k)} = \sum_{i=1}^{|D|} q \cdot e^{-\frac{|x^{(i)} - x^{(k)}|}{\sigma_d}}. \quad (10)$$

Associating the sensors to be placed as negative charges, the virtual charge  $q$  has to be negative as well. In the current implementation, we assign the same repulsive force to all previous measurements and select  $q = -1$ . Finally, the APF contributions are additively combined with importance factors  $\beta_M$ ,  $\beta_V$ , and  $\beta_R$  for each objective:

$$APF^{(k)} = \beta_M APF_M^{(k)} + \beta_V APF_V^{(k)} + \beta_R APF_R^{(k)}. \quad (11)$$

Finally,  $n_{sp}$  locations are identified iteratively by selecting the location at which the potential takes its minimum as a suggested measurement point and updating the APF by temporarily placing an additional measurement charge at the selected location. Theoretically it could happen that the attractive forces towards an increased mean in one direction and towards and increased variance in the opposite direction cancel themselves out. In practice, we did not observe such

an effect. It is unlikely that the attractive forces are completely balanced at the position of the sensor, and if they are not the sensor will be directed towards one of the directions so that in the next step the symmetry is broken.

### C. Selection of the Next Measurement Location

The sensor planning approach detailed in the previous section distributes its suggestions over the target area without any spatial order. Moving the mobile gas sensor directly to these locations could create a seesaw movement, which tends to empty the batteries sooner, resulting in fewer measurements. Therefore, we add a locality constraint by selecting out of the  $n_{sp}$  suggestions from the sensor planning component the *most often suggested close-by* measurement location. This is implemented by a matrix  $S$  that has the same discretization as the gas distribution model. For each grid cell  $S^{(k)}$  it counts how often the cell was suggested since it was actually visited the last time. The next measurement point is ultimately selected as the one with the highest ratio  $S^{(k)}/d(k)$ , where  $d(k)$  is the distance between the current position of the sensor and grid cell  $k$ . Thus, a location far away from the current position will only be selected if it is frequently suggested.

In the current implementation, we increase not only the counter for a suggested cell but also the counter of neighboring cells within a radius of 0.5 m by one, which corresponds to the scale of the drainage area below the drone (that has a diameter of 1m).

### D. Path Planning Algorithm for the Micro-Drone

The initial measurement location is chosen randomly in the target area. Then the following steps are iteratively performed:

- collect gas sensor and wind measurements while keeping the drone at a fixed position for a prolonged time (here: 20 s);
- average the wind measurements over the measurement time (20s);
- compute the predictive gas distribution model using the Kernel DM+V/W algorithm (Sec. II.A), the input to the algorithm are the current positions and gas sensor readings and the averaged wind measurement;
- derive an estimate of the source location from the predictive gas distribution map (detailed below);
- determine the  $n_{sp}$  suggested sampling locations with the APF based sensor planning component (Sec. II.B);
- update the matrix  $S$  and select a sampling location that maximizes the ratio  $S^{(k)}/d(k)$  as described in Sec. II.C;
- fly the drone autonomously to the chosen sampling location and repeat with the first step. (Measurements in between two sampling locations are not used to decrease the influence of a memory effect in the sensor response due to the slow sensor recovery.)



Fig. 1. Pollution source and micro-drone during one of the experiments.

The algorithm terminates either if the battery runs out or the confidence map  $\alpha^{(k)}$  is above a defined threshold for each cell  $k$ .

## III. ROBOTIC PLATFORM

Federal Institute for Materials Research and Testing (BAM), in cooperation with Airrobot GmbH & Co. KG, has developed a mobile and flexible measurement system as part of an R&D project funded by the Federal Ministry of Economics and Technology [2], [3], [4]. The result of the project is a gas-sensitive sensor module (approx. 200 g) for the Airrobot drone AR100-B (Fig. 1). The drone can be flown by line of sight, via onboard video camera and video goggles as well as by autonomous waypoint tracking.

The Inertial Measurement Unit (IMU) is an important part of the drone. It provides the basis for flight control and wind vector estimation and can be read out during operation. The IMU consists of three orthogonally arranged accelerometers, which detect linear accelerations along the  $x$ -,  $y$ - and  $z$ -axis, and three orthogonally arranged rotation rate sensors, which measure angular accelerations along the  $x$ -,  $y$ - and  $z$ -axis. Magnetic field sensors (compass) and GPS are used to improve the accuracy of the IMU and to compensate for sensor drift. The IMU of the drone also contains a barometric pressure sensor to control the drone's altitude.

A commercially available gas detector (Dräger X-am 5600), which was originally designed as a handheld device for personal safety, is the base unit of the gas sensitive payload. Depending on the scenario, it can measure many combustible gases and vapors with the catalytic sensor as well as different (toxic) gases, e.g.  $O_2$ ,  $CO$ ,  $H_2S$ ,  $NH_3$ ,  $CO_2$ ,  $SO_2$ ,  $PH_3$ ,  $HCN$ ,  $NO_2$ , and  $Cl_2$  with electrochemical and infrared sensors.

An additional electronic circuit controls the communication between the gas detector and the drone via appropriate device interfaces. A temperature and humidity sensor was also integrated as both factors may affect the measurement data (however, no compensation for varying temperature or humidity was applied in the experiments presented in this paper). The casing of the gas detector is protected against water and dust according to IP 67 (see [5] for further information) and therefore capable of working outdoors.

#### IV. EXPERIMENTAL SETUP

All experiments were carried out inside an  $8 \times 12 \text{ m}^2$  area in an outdoor environment with a micro-drone equipped with electrochemical CO sensors. Gas concentration and wind measurements were recorded with 1 Hz. Measurements were taken at each measurement position for about 20 s, which is of the same order as the  $T_{90}$  response times of the used sensors. The wind vector was then averaged over all the measurements collected at the measurement point. Each gas sensor measurement was then included into the gas distribution model as if it was acquired together with a measurement of the average wind vector, i.e. the average wind vector was used for all individual gas sensor measurements acquired at the measurement position.

The parameters of the Kernel DM+V/W algorithm were heuristically set to  $c = 0.15 \text{ m}$  (grid cell size),  $\sigma = 0.40 \text{ m}$  (kernel width),  $\sigma_{\Omega} = N(0, \sigma = 0.4) \approx 1.0$ , and  $\gamma = 0.2 \text{ s}^{-1}$ . Equal importance factors  $\beta_M$ ,  $\beta_V$ , and  $\beta_R$  were chosen for the APF contributions. The flight speed of the drone between the measurement positions was set to  $1 \text{ ms}^{-1}$ . Because of the low flight height of about 1 m, the height of the drone was controlled manually during the experiments. Each run took around 14 – 19 minutes to complete. A barbecue filled with burning coal and fresh, damp wood was used as a pollution source (Fig. 1) and was placed approximately in the middle of the experimental area (at approx. (6.3, 3.8) m from the bottom left corner). The drone was set to autonomous waypoint mode directly after take-off, which started the experiment.

#### V. RESULTS

The results presented in Fig. 2 and Table I demonstrate the suitability of the proposed algorithm for gas distribution mapping and its use for localization of a stationary gas source. Table I shows for all five runs the distance between the true gas source location and three different estimates after the last measurement point. The first estimate is derived by selecting grid cells in which the predictive mean is larger than 90% of the maximum. The center of this area is taken as the source location estimate and the maximum extension in  $x$ - or  $y$ -direction is used to specify a confidence interval. In the same way the other two estimates are computed using the variance (second result) or the product of mean and variance (third result). The true source location was within the mean estimation area only in one trial and within the variance estimation area in two trials. This is in line with previous

TABLE I  
RESULTS OF THE EXPERIMENTS

run	measurement points	distance to true source location,		
		estimate using mean / variance / mean-variance		
1	27	(1.66±0.75) m	(1.52±0.71) m	(1.57±0.50) m
2	24	(2.64±0.65) m	(2.84±0.68) m	(2.75±0.46) m
3	31	<b>(0.68±0.77) m</b>	<b>(0.25±0.80) m</b>	<b>(0.46±0.57) m</b>
4	20	(3.01±2.43) m	(2.05±0.89) m	(1.89±0.64) m*
	34	(1.84±1.32) m	(2.51±0.50) m	(2.28±0.49) m
5	32	(1.72±0.80) m	<b>(0.74±0.86) m</b>	(1.41±0.55) m

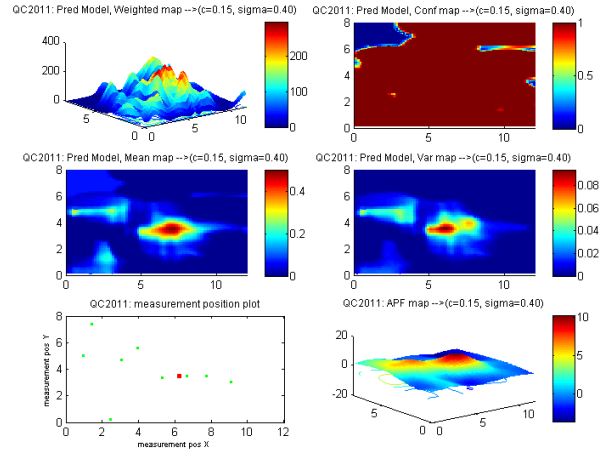


Fig. 2. The top row shows the weight map  $\Omega^{(k)}$  (left) and the confidence map  $\alpha^{(k)}$  computed with the Kernel DM+V/W algorithm (right). The middle row shows the corresponding mean distribution map  $r^{(k)}$  (left) and variance distribution map  $v^{(k)}$  (right). Bottom row, left: area with the suggested next measurement points (green dots) and the source location estimate (red dot). Bottom row, right: visualization of the APF. All plots were created after the last time step of the SP algorithm (run 3, measurement 31).

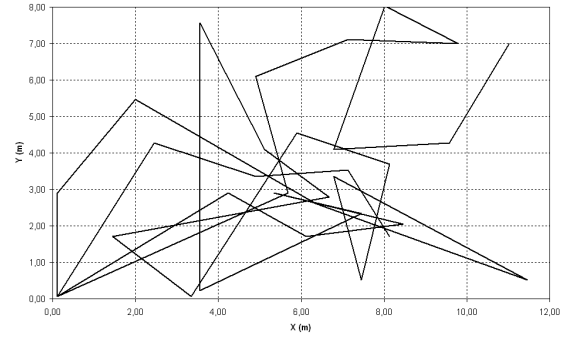


Fig. 3. Calculated sample trajectory of the SP algorithm (run 3) with starting position  $(x, y) = (11.02, 7.00) \text{ m}$ .

observations that the concentration variance often provides a better indication of the gas source location [8] than the mean.

Fig. 2 shows the final snapshot of run number 3 after 31 measurement points. The first four diagrams are related to the Kernel DM+V/W algorithm and show the weight map  $\Omega^{(k)}$ , the confidence map  $\alpha^{(k)}$ , the mean distribution map  $r^{(k)}$ , and the variance distribution map  $v^{(k)}$ . The last two diagrams show the measurement positions suggested by the sensor planning component (green dots) together with the predicted source location (red dot) and the APF map. Fig. 3 shows exemplarily the trajectory produced by the SP algorithm in run 3 with starting position  $(x, y) = (11.02, 7.00) \text{ m}$  (compare with Fig. 2).

Keeping the gas emission rate constant over time with the chosen gas source was difficult. A re-ignition of the almost extinguished source in run #4 for example (after the 20th measurement) created an intense emission that likely caused very high concentrations also far away from the source. The 21st measurement taken at position  $(x, y) = (8.85, 4.95) \text{ m}$  was affected by this outburst, which caused a strong change in the gas source location estimate and is therefore. Results

are given in Table I for the 20 measurement points up to this event, marked with an asterisk (\*), and for the full duration of the experiment. Another difficulty, which should be mentioned here, is the slow sensor decay. Flying from one measurement position to another directly over the source can also lead to wrong source estimates when the sensor still responds to the high concentrations close to the source.

## VI. CONCLUSIONS AND FUTURE WORK

Statistical gas distribution modelling indicates areas of high mean and variance and the respective maxima suggest areas that are good candidates for further inspection. The proposed APF-based approach balances objectives related to exploration and exploitation. The repulsive part prevents repeated measurements at the same locations and thus promotes exploration. The attractive part directs the attention to areas for which higher gas accumulation or higher variance in the predictive gas dispersion is predicted (exploitation). Through the introduction of a locality constraint, implemented by selecting in each step the most often suggested close-by measurement location, the results of the sensor planning component could be used to plan suitable paths for a mobile gas sensor. The proposed algorithm was tested in real-world experiments with a gas sensitive micro-drone. The initial results presented in this paper show the potential of this approach for gas distribution mapping and highlight that the produced maps can provide good estimates of the gas source location.

The method presented in this paper leaves ample room for future work. With respect to real-world applications, it should be investigated how robust the proposed approach is with respect to changing wind directions and to different levels of turbulence.

The current implementation does not take into account the time when the measurements were made. We will study therefore an extension of the approach proposed in this paper that introduces time-dependency at two points. First, a time dependent statistical gas distribution modeling algorithm will be used, for example the Time-Dependent (TD) Kernel DM+V/W algorithm introduced in [9]. Second, the charge  $q$  that scales the strength of the repulsive potential exerted from previous measurement points should also be time-dependent, namely it should be lower for earlier measurements. We also plan to study an extension to a 3D approach.

Finally, we will investigate methods to select optimal relative weights ( $\beta$  parameters) for the different objectives in Eq. (11), and include more real-world experiments and simulations to test the algorithm.

## ACKNOWLEDGMENT

The authors thank the participating colleagues from BAM and Örebro University. The authors also would like to express their gratitude to BMWi (MNPQ Program; file

number 28/07) and to the EC (contract number FP7 – 224318 - DIADEM: Distributed Information Acquisition and Decision-Making for Environmental Management) for funding the research.

## REFERENCES

- [1] Kowadlo, G.; Russell, R. A.: Robot Odor Localization: A Taxonomy and Survey. *In: Int. J. Rob. Res.* 27 (2008), Nr. 8, S. 869 – 894.
- [2] Neumann, Patrick P.; Bartholmai, Matthias; Schiller, Jochen H.; Manolov, Manol; Wiggerich, Burkhard: Self Optimizing Search and Characterization of Gaseous Hazardous Substance Sources using a Micro-Drone: A new Approach to determine Wind Speed and Direction. *IEEE International Workshop on Robotic and Sensors Environments (ROSE 2010)*, Phoenix, AZ, USA.
- [3] Neumann, Patrick; Bartholmai Matthias: Self Optimizing Search and Characterization of Gaseous Hazardous Substance Sources using a Micro-Drone. *Proceedings of the International Micro Air Vehicle Conference and Flight Competition (IMAV)*, 2010.
- [4] Bartholmai, Matthias; Neumann, Patrick: Micro-Drone for Gas Measurement in Hazardous Scenarios via Remote Sensing. *Proceedings of the 6th International Conference on REMOTE SENSING (REMOTE'10)*, Iwate, Japan.
- [5] ANSI/IEC 60529-2004: *Degrees of Protection Provided by Enclosures (IP Code)*. National Electrical Manufacturers Association, Virginia.
- [6] Reggente, Matteo; Lilienthal, Achim J.: Using Local Wind Information for Gas Distribution Mapping in Outdoor Environments with a Mobile Robot. *Proceedings of IEEE Sensors, 2009*, 1715 – 1720.
- [7] Reggente, Matteo; Lilienthal, Achim J.: The 3D-Kernel DM+V/W Algorithm: Using Wind Information in Three Dimensional Gas Distribution Modelling with a Mobile Robot. *Proc. IEEE Sensors, 2010*, pp. 999-1004.
- [8] Lilienthal, Achim J.; Duckett, Tom; Werner, Felix and Ishida, Hiroshi: Indicators of Gas Source Proximity using Metal Oxide Sensors in a Turbulent Environment. *Proc. IEEE / RAS-EMBS Int. Conf. on Biomedical Robotics and Biomechatronics (Biorob)*, 2006.
- [9] Asadi, Sahar; Pashami, Sepideh; Loutfi, Amy and Lilienthal, Achim J.: TD Kernel DM+V: Time-Dependent Statistical Gas Distribution Modelling on Simulated Measurements. *Olfaction and Electronic Nose - Proceedings of the 14th International Symposium on Olfaction and Electronic Nose (ISOEN)*, 2011, to appear.